PCCP

ROYAL SOCIETY OF CHEMISTRY

PAPER

View Article Online
View Journal | View Issue

Cite this: *Phys. Chem. Chem. Phys.*, 2026, **28**, 2725

Computational insights into the structural and electronic properties of first-row transition metal-doped In_2O_3 systems

Ling Meng,[ab] Francesc Viñes [a] and Francesc Illas [a]*

Received 24th November 2025,
Accepted 5th January 2026

DOI: 10.1039/d5cp04556h

rsc.li/pccp

Indium oxide (In_2O_3) has emerged as a promising catalyst for CO_2-to-methanol conversion, although its efficiency is limited by poor H_2 activation. Inspired by recent findings that economical Co-doping enhances the catalytic performance of In_2O_3, this study employs density functional theory (DFT) to systematically investigate the structural and electronic properties of first-row 3d transition metals (TM = Sc, Ti, V, Cr, Mn, Fe, Co, Ni, Cu, Zn) doped In_2O_3, aiming to guide rational catalyst design. The present analysis shows that the electronic configuration of the TM dopant plays a critical role in determining its preferred doping site, formation energy, charge transfer, and electronic distribution. Overall, early transition metals (TMs) exhibit lower formation energies and thus higher thermodynamic stability, whereas late TMs involve higher formation energies. A strong linear correlation between formation energy and Bader charge transfer indicates that electron-donating ability is the dominant factor governing doping stability, whereas the correlation with the d-band center is moderate. The analysis of the projected density of states (PDOS) reveals that metals with partially d filled orbitals contribute significantly near the Fermi level, E_F, which may enhance the electron transfer and catalytic activity. In contrast, metals with fully filled d orbitals display negligible contribution. This systematic screening of dopants offers a general strategy to enhance In_2O_3 catalytic performance and provides a theoretical foundation for the rational design of cost-effective catalysts.

1. Introduction

The increasing concentration of atmospheric carbon dioxide (CO_2) constitutes a critical issue for both global warming and climate change, which triggered several strategies aimed at mitigating them.[1,2] Carbon capture and utilization (CCU) technologies emerged as a promising approach to use atmospheric CO_2 as an input feedstock for chemical processes leading to useful chemical commodities such as carbon monoxide (CO), formic acid (HCOOH), and methanol (CH_3OH),[3–6] which constitute chemical precursors for the synthesis of more complex chemicals and fuels. In particular, methanol, obtained from CO_2 hydrogenation, is of interest because of its use as a bulk chemical in the industry to produce, among others, olefins, acetic acid, and formaldehyde,[7,8] or as a potential green fuel,[9] provided the used hydrogen is also obtained from green sources.[10,11]

Despite the possible benefit of the direct catalytic hydrogenation of CO_2 to methanol, a large scale implementation of the process remains hindered because of the CO_2 high thermodynamic stability and its concomitant problems from the kinetic point of view.[12] Clearly, CO_2 conversion requires active and, more important, selective catalysts able to conduct the reaction of interest under relatively mild working conditions of temperature and pressure.[13] In this sense, metal oxides[14,15] have attracted considerable attention due to their unique chemistry arising from the presence of different facets and/or of defects such as oxygen vacancies, as elegantly explained by Pacchioni several years ago.[16] Among the vast family of metal oxides, indium oxide (In_2O_3) is of particular interest because of its ability to selectively catalyze CO_2 hydrogenation to methanol production, even at rather high working temperatures.[17,18] Nevertheless, some issues still remain as open questions, since Cannizzaro *et al.*[19] demonstrated that, even though In_2O_3 exhibits excellent selectivity for methanol by effectively suppressing the competing reverse water–gas shift (RWGS) reaction, the overall CO_2 conversion remains limited due to the low ability of this oxide to activate and dissociate molecular hydrogen (H_2), which in turn hampers its catalytic efficiency for CO_2 hydrogenation to methanol.

[a] *Departament de Ciència de Materials i Química Física & Institut de Química Teòrica i Computacional (IQTCUB), Universitat de Barcelona, c/Martí i Franquès 1-11, 08028, Barcelona, Spain. E-mail: francesc.illas@ub.edu*

[b] *State Key Laboratory of Chemical Resource Engineering, Beijing Engineering Center for Hierarchical Catalysts, College of Chemistry, Beijing University of Chemical Technology, Beijing 100029, China*

To overcome the poor performance of In_2O_3 towards hydrogen dissociation, several strategies have been explored.[20,21] These involve either metal doping or combining In_2O_3 with other metal oxides.[22] At present, most studies have focused on metal doping because this can enhance catalytic performance by tuning the electronic structure, redox behavior, and defect properties of the material.[23,24] For instance, Dostagir *et al.*[25] reported that Rh-doped In_2O_3 exhibits significantly higher CO_2 conversion and methanol selectivity; while Liu *et al.*[26] showed that a small amount of Pd doping into the In_2O_3 enables CO_2 electroreduction to ethanol with a high Faraday efficiency at a low overpotential, suggesting that the conversion to ethanol is promoted by regulating the adsorption free energy of the CO intermediate. In both examples, expensive scarce metals are employed which claim for more economical and plausible alternatives.

Recently, it has been shown that doping In_2O_3 with cobalt (Co) does not only improve the catalytic activity of the host oxide, but also maintains, or even enhances, its selectivity towards methanol.[27,28] To shed light into the effect of Co doping in the properties of In_2O_3, Voccia *et al.*[29] explored the properties of Co-doped In_2O_3 combining experimental characterization and density functional theory (DFT) simulations. The author addressed several key aspects, including the effect of the presence of Co on the crystal lattice and electronic band structure, the oxidation state of Co in the doped system, and the impact of Co on the oxygen vacancy formation energy. More recently, Kapse *et al.* have shown that the presence of Co induces significant changes in the molecular mechanism of CO_2 hydrogenation, thus explaining the origin of the experimentally observed catalytic activity.[30]

Despite promising results obtained with Co-doped system, a fundamental question remains unresolved; whether other inexpensive 3d transition metals can achieve comparable or superior performance, crucial for guiding the rational design of economical In_2O_3-based catalysts. To this end, the present study aims to go beyond previous works considering just the effect of Co and systematically investigating the doping by the complete series of first-row transition metal dopants. By means of suitable density functional theory (DFT) based calculations, a series of properties such as the preferred doping site, the doping stability, the dopant Bader charge, and the effect on the density of states (DOS) are systematically evaluated. The outcome of this comprehensive investigation provides a deeper understanding of the role of dopants in modulating In_2O_3-based catalytic performance, while offers a valuable guidance for the rational design of efficient and economically viable catalysts for CO_2 hydrogenation to methanol. Simultaneously, DFT-based first-principles calculations serve as a powerful complement to experimental studies, providing atomic-level insights into structure–property relationships that are difficult to capture experimentally, thereby guiding the rational design of catalysts in materials science.

2. Computational details

All results reported in the present work have been extracted from DFT based calculations carried out using periodic models optimized by the Vienna *ab initio* simulation package (VASP).[31,32] The total energy and concomitant electronic structure was obtained using the Perdew–Burke–Ernzerhof (PBE)[33] exchange–correlation functional within the generalized gradient approximation (GGA), which has been shown in previous studies to reliably describe the structural and bonding energy characteristics of In_2O_3 systems.[29,34] Here it is worth pointing out that it is well known that GGA functionals tend to underestimate the bandgap as predicted from the band structure.[35] This shortcoming can be overcome by using more sophisticated hybrid functionals introducing a fraction of non-local Fock exchange,[35–37] such as Heyd–Scuseria–Ernzerhof functional (HSE06). However, this significantly increases the computational cost, especially for large unit cells and a plane-wave basis set as used in this work. Moreover, the amount of Fock exchange appears to be rather material dependent,[38] which confers a semiempirical flavor to this approach. For a screening-oriented study, relative energy trends are more important than absolute values. Single-point calculations with the HSE06 functional based on PBE-optimized structures were performed on randomly selected dopants (Cu, Zn, Cr, and Sc), the results show that despite differences in absolute formation energies, the relative energy trends are completely consistent, as shown in Fig. S1 in SI. Using PBE is therefore a reasonable choice for this study. Thus, PBE functional can be regarded as suitable for this study.

A possible alternative is to make use of the include the so-called Hubbard U term correction term (*i.e.*, the PBE + U method),[29,39] which, nonetheless, implies a semiempirical approach as well. In this work, we uniformly adopt the PBE method (without U) for all calculations. This choice is justified because this study focuses on the trends in the impact of different transition metal doping on thermodynamic stability and related electronic properties, rather than on the precise band structure or local magnetic moments, and, on the other hand, the choice of U values varies widely across different transition metals and literature sources, which could introduce artifact, systematic errors and hamper the possibility to carry out a sound comparison since, *de facto*, each systems would be treated with a different method. Finally, the previous work for Co-doped In_2O_3[29] has shown that PBE calculations qualitatively reproduce the main electronic structure features of this system, which is sufficient for the present purposes aimed at disclosing trends in In_2O_3 doped by 3d transition metals rather than scrutinizing the precise electronic details of each system. Besides, PBE is more computationally efficient and, hence, a suitable reasonable choice for large-scale screening.

The valence electron density is expanded in a plane wave basis set, with a kinetic energy cutoff of 415 eV, and the interaction between core electrons and valence electrons is accounted for through the projector augmented wave (PAW) method.[40,41] The convergence threshold for the electronic self-consistency process is set to 10^{-5} eV, and structural optimization is continued until the residual forces on all atoms are less than 0.01 eV $Å^{-1}$. For Brillouin zone integration, a $3 \times 3 \times 3$ Monkhorst–Pack k-point grid centered at the Γ point is used. To account for long-range van der Waals interactions, the

dispersion was accounted for in all calculations by means of the original D3 method with zero damping proposed by Grimme *et al.*[42] In addition, Gaussian smearing was employed for total energy and density of states (DOS) calculations to ensure accurate energy convergence and smooth DOS curves. Considering that all dopants involve open shells, all calculations were carried out including spin polarization.

Phonon calculations were also performed to evaluate the dynamic stability of the doped In_2O_3 systems. The structures were further optimized before the phonon calculations, with a stricter electronic convergence criterion of 1×10^{-8} eV and force on all atoms less than 0.001 eV Å^{-1}. The phonon spectra were obtained using the finite-displacement method as implemented in the PHONOPY package.[43]

The most stable form of the In_2O_3 bulk structure used in this study is the body-centered cubic (*bcc*) bixbyite[44,45] crystal structure, composed of 80 atoms (see Fig. 1). There are 48 oxygen atoms and two types of In atoms in different local environments, labeled as In_1 and In_2, with 8 In_1 atoms and 24 In_2 atoms.

To evaluate the stability of different neutral metal atoms doped into the In_2O_3 lattice, we define the formation energy, ΔE_f, of the doped system, as:

$$\Delta E_f = E_{In_2O_3+M} + E_{In} - E_{In_2O_3} - E_M \quad (1)$$

where $E_{In_2O_3+M}$ is the total energy of the metal doped-In_2O_3 lattice with the M atom substituting an In atom on the lattice, $E_{In_2O_3}$ is the total energy of the In_2O_3 cell, E_{In} is the energy of a single In atom, referenced to the energy of bulk In, and E_M is the energy of a doping metal atom, also referenced to the energy of M bulk.

In addition, we also considered the cohesive energy, E_{coh}, to evaluate the stability of the doped systems, as follows:

$$E_{coh} = \frac{(N_M \cdot E_M + N_{In} \cdot E_{In} + N_O \cdot E_O) - E_{In_2O_3+M}}{N_{total}} \quad (2)$$

here, N_M, N_{In}, and N_O represent the numbers of doped metal, In, and O atoms in the doped supercell, respectively. E_M, E_{In}, and E_O denote the energies of isolated doped metal, In, and O atoms. $E_{In_2O_3+M}$ is the total energy of the metal-doped In_2O_3 lattice with the M atom substituting an In atom, similar to eqn (1). N_{total} is the total number of atoms in the studied system. To clearly show the effect of the dopant on the cohesive energy, the difference between the values for the undoped and doped systems, ΔE_{coh}, is also considered.

We note here that using the bulk reference avoids the problems related to the use of a single Slater determinant to approach the open shell multiple ground state of atoms and, also, the use of a broken symmetry solution and the incorrect occupancy of predicted by PBE for some atoms.[46] Note also that the energy formation with respect to the gas phase atoms can be readily obtained from the cohesive energy of the metal taken from calculations or from experiment (see *e.g.* ref. 47 and 48). With this definition, a negative value of ΔE_f indicates that doping is energetically favorable. Finally, to understand the main effects of doping on chemical features we rely on Bader charges and DOS analysis.

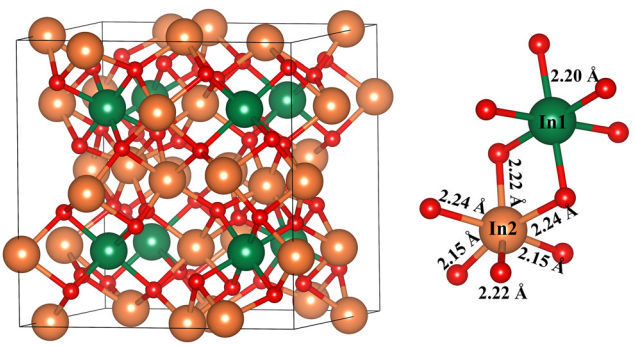

Fig. 1 The most stable crystal structure of *bcc* In_2O_3, consisting of 80 atoms with 32 In and 48 O atoms (left). The 32 In atoms are further classified into 8 In_1 and 24 In_2 atoms (right), represented by green and orange spheres respectively, while oxygen atom is shown as red spheres.

3. Results and discussion

3.1. Doping sites preference and electronic properties

As above stated, in bulk In_2O_3 bixbyite phase there are two different In sites; In_1 and In_2. The O atoms coordination environment around In_1 differs from that around In_2 (*cf.* Fig. 1), which may lead to a preference for the doping transition metal (TM) atoms to occupy different positions. The optimized lattice parameters are consistent with previously reported values with deviations of at most 0.040 Å, and also a good agreement with experimental data derived from XRD measurements, with 0.063 Å.[29] Here we first systematically investigated the stability of the first-row TMs (TM = Sc, Ti, V, Cr, Mn, Fe, Co, Ni, Cu, Zn) when substituting the In_1 and In_2 sites, which ultimately defines the subsequent doping effects. The ΔE_f is a key indicator of the thermodynamic stability of the doping process, and the gained results are shown in Table 1, revealing that most TMs (*i.e.* Sc, Ti, V, Mn, Ni, and Zn) preferentially occupy the In_2 site, while Cr, Co, Fe, and Cu tend to be favored on the In_1 site—consistent with previous finding for Co.[29]

This site preference is likely to be governed by the interplay between the electronic configuration of dopant and the local symmetry of the host sites. The In_1 site, with six equivalents In–O bonds, provides a highly symmetric octahedral environment that may better accommodate metals with an electron configuration with single s orbital occupancy and half-filled or fully filled d-shells, such as Cr and Cu with Ar[$4s^1 3d^5$] and Ar[$4s^1 3d^{10}$] electron configuration, respectively, as well as metals with a relatively high number of d-electrons such as Co and Fe with Ar[$4s^2 3d^7$] and Ar[$4s^2 3d^6$] electron configuration, respectively.

In contrast, the lower symmetry and distorted site of In_2 site may allow more structural flexibility, stabilizing other dopants. For instance, Mn and Zn with an electron configuration with fully filled 4s orbitals may likely prefer In_2 site. This observation suggests that, in addition to the occupancy of the d orbitals, the occupancy of the s orbitals may also influence the doping site in In_2O_3. Nevertheless, one must note that the electron

Table 1 Ground state electronic configuration of the isolated atom, preferred doping site (In_1/In_2), ΔE_f (eV), ΔE_{coh} (eV), Bader charge, Q (e), d-band center, ε_d, in eV, local magnetic moment (μ_{local}, μ_B) and total magnetic moment (μ_{total}, μ_B) of the first-row transition metal doped In_2O_3 systems

M	Electronic configuration	Doping site	ΔE_f	ΔE_{coh}	Q	ε_d	μ_{local}	μ_{total}
Sc	$[Ar]4s^23d^1$	In_2	−6.72	0.01	2.04	5.51	0	0
Ti	$[Ar]4s^23d^2$	In_2	−5.59	0.03	2.17	0.31	0	0
V	$[Ar]4s^23d^3$	In_2	−3.15	−0.03	1.80	1.01	1.40	1.38
Cr	$[Ar]4s^13d^5$	In_1	−2.64	0.01	1.76	0.11	2.75	2.75
Mn	$[Ar]4s^23d^5$	In_2	−1.63	0.02	1.62	−0.40	3.58	3.71
Fe	$[Ar]4s^23d^6$	In_1	0.28	0.00	1.45	−0.41	1.26	1.23
Co	$[Ar]4s^23d^7$	In_1	0.32	0.08	1.30	−0.34	0	0
Ni	$[Ar]4s^23d^8$	In_2	1.15	0.09	1.25	−1.22	0.74	0.95
Cu	$[Ar]4s^13d^{10}$	In_1	1.66	0.06	1.27	−2.84	0.83	1.82
Zn	$[Ar]4s^23d^{10}$	In_2	0.26	−0.04	1.33	−4.19	0.02	0.02

configuration of the dopant in the host crystal is for sure different from that in vacuum as evidenced by the Bader charges in Table 1. Hence, the reasoning arguments above have to be taken with a grain of salt, and just as a first qualitative interpretation, because the doping site preference for first-row transition metal dopants in In_2O_3 is a complex process involving multiple factors going from the electronic structure of the metal, to the symmetry and geometric configuration of the doping site.

3.2. Stability and Bader charge analysis

The ΔE_f shown in Table 1 and Fig. 2 reveal that ΔE_f increases steadily from Sc to Zn, indicating a gradual decrease in the easiness of doping across the series. For Sc to Mn, the formation energies are negative (−6.72, −5.59, −3.15, −2.64 and −1.63 eV for Sc, Ti, V, Cr, and Mn, respectively), decreasing in magnitude with increasing the atomic number. This supports that doping with this early transition metal (Sc, Ti, V, and Cr) is thermodynamically favorable, while Mn marks the transition towards the energetically unfavorable late transition metals. In contrast, the formation energies from Fe to Zn are all positive (0.28, 0.32, 1.15, 1.66, and 0.26 eV for Fe, Co, Ni, Cu, and Zn, respectively), indicating that these doped systems have limited thermodynamic stability.

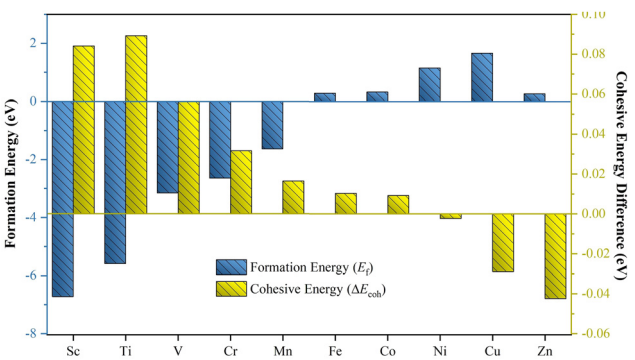

Fig. 2 Formation energies (E_f) and cohesive energies (E_{coh}) of In_2O_3 doped with first-row 3d TMs. E_f and E_{coh} correspond to the blue and yellow squares, respectively.

Similarly, the local site symmetry and geometry of the In_2O_3 lattice may also influence the dopant formation energies. Metals that prefer the higher-symmetry In_1 site (Fe, Co, Cu) generally exhibit higher ΔE_f than those favoring the lower-symmetry In_2 site (Sc, Ti, V, Mn, Zn), supporting the interpretation that site symmetry and local geometry significantly influence the doping atom stability.

Notably, Zn shows a relatively low formation energy (0.26 eV) compared to those of elements ranging from Fe to Cu, deviating from the general increasing trend. This anomaly may be attributed to the unique fully filled $4s^23d^{10}$ electronic configuration of Zn, which may result in different charge transfer behavior or bonding with oxygen atoms when interacting with the In_2O_3 lattice. Beyond the influence of electronic configurations, dispersion interactions also contribute to the dopant formation energies. Without including dispersion through the DFT-D3 method, Fe (2.57 eV) was predicted as the most stable, followed by Co (2.63 eV) and Zn (2.70 eV). However, the $3d^{10}$ closed-shell configuration of Zn makes it more responsive to dispersion interactions, resulting in a stability gain of −2.44 eV compared to the open-shell Fe (−2.29 eV) and Co (−2.31 eV), as shown in Fig. S2 in SI. This small difference in correction was sufficient to reverse their stability order, leading to the ordering Zn < Fe < Co.

In addition to the ΔE_f, which reflects the feasibility of doping, we also analyzed the cohesive energy, E_{coh}, to evaluate the structural stability of the doped systems. As shown in Table 1 and Fig. 2, all doped systems exhibit high cohesive energies within a narrow range (4.68 eV per atom for Zn to 4.81 eV per atom for Ti), indicating that they are all robust and structurally stable. Furthermore, since Sc-doped In_2O_3 was identified as the most thermodynamically stable system (ΔE_f = −6.72 eV), we further assessed its dynamic stability through specifically including phonon calculations. The obtained phonon band structure shows no imaginary frequencies throughout the entire Brillouin zone, as displayed in the left panel of Fig. 3, which is consistent with the phonon density of states (DOS) shown in the right panel. The corresponding reciprocal space and the high-symmetry k-paths of Γ—X—Y—Γ—Z—R—Γ—T—U—Γ—V are shown in Fig. S3 of the SI. These results confirm the dynamic stability of the Sc-doped In_2O_3 system. Meanwhile, the phonon-derived thermodynamic properties of the system were also calculated (Fig. S4 of the SI). As the temperature increases, the free energy decreases while the entropy increases, consistent with thermodynamic principles. In addition, the heat capacity (C_v) at constant volume was calculated using the well-known relation (eqn (3)) implemented in PHONOPY program,[43]

$$C_v = R\int_0^{\omega_{max}} \left(\frac{\hbar\omega}{k_B T}\right)^2 \frac{e^{\frac{\hbar\omega}{k_B T}}}{\left(e^{\frac{\hbar\omega}{k_B T}} - 1\right)} g(\omega)\mathrm{d}\omega \qquad (3)$$

where g is the phonon DOS, ω denotes the vibrational frequency, R, k_B, and T stand for the gas constant, Boltzmann constant, and temperature, respectively. The results showed

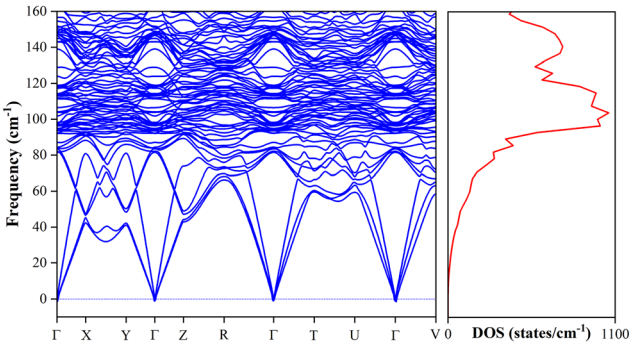

Fig. 3 Phonon band structure of Sc-doped In_2O_3 along high-symmetry paths of the Brillouin zone (left panel), and its corresponding phonon density of states (DOS) (right panel).

that the C_v rises with temperature and becomes nearly unchanged above about 400 K, showing thermodynamically reasonable behavior.

In addition to thermodynamic and dynamic stability analyses, we performed a systematic spin-polarization analysis to investigate the intrinsic electronic structure and spin polarization effects of the TM dopants. The magnetic moments, μ_B, are characterized by local magnetic moments (μ_{local}) for doped metal atom, and the total magnetic moment (μ_{total}) for the entire unit cell, with results summarized in Table 1. The results show that the magnetic behavior strongly depends on the dopant. Sc, Ti, Co, and Zn converged to a non-magnetic ground state ($\mu_{total} \approx 0\mu_B$), which is physically sound, as Sc ($3d^1$) and Ti ($3d^2$) readily lose their few d-electrons to the surrounding oxygen atoms, allowing them to achieve a stable, non-magnetic d^0 ionic state. In contrast, Zn possesses a stable $3d^{10}$ closed-shell configuration, which is difficult to lose these paired d-electrons, also resulting in no magnetic moment. Whereas Co ($3d^7$) is a special case, adopting a stable low-spin state in In_1 site, which leads to a zero net moment. In contrast, V, Cr, Mn, Fe, Ni, and Cu all exhibited magnetic ground states due to unpaired d-electrons, with strongly localized magnetic moments close to their total moments ($\mu_{local} \approx \mu_{total}$). However, for systems like Cu, the total moment ($\mu_{total} \approx 1.82\mu_B$) is significantly larger than the local moment ($\mu_{local} \approx 0.83\mu_B$), indicating a strong spin polarization of the surrounding O atoms in the In_2O_3 lattice.

Finally, to further understand the behavior of metal dopants in the In_2O_3 lattice, we analyzed in detail the trends of the Bader charges reported in Table 1. In all cases, there is clear trend to transfer electrons from the metal atom to the host oxide, so that the dopant gets positively charged, as expected from the rather high ionic character of the chemical bonding in In_2O_3.[49] Nevertheless, results in Table 1 indicate that the doped metal atoms exhibit markedly different charges. For instance, Ti shows the largest +2.17e charge, forming strong coulombic interactions with the surrounding O atoms of the In_2O_3 lattice, in line with the strong ionic character of the host crystal. Nevertheless, rather large differences are encountered along the 3d series with dopants such as Ni and Cu being less charged; +1.25 and +1.27e, respectively, likely due to a trend to keep the d shell almost filled.

To better understand these trends, the correlation between the formation energies and the Bader charges of the doped metal atoms was analyzed in Fig. 4, revealing a strong linear relationship with a regression coefficient of R = 0.974. This indicates that the amount of charge transferred from the dopant atom plays a key, determining role. Thus, a larger electron transfer is directly associated with a lower (more negative) formation energy, implying an enhanced thermodynamic stability. In contrast, those dopant metal atoms that transfer fewer electrons tend to exhibit higher (more positive) formation energies, indicating a reduced stability of the doping process.

3.3. Electronic structure analysis

A better picture of the electronic structure changes induced by dopant metal atoms can be gained from the DOS analysis, specially when projected on the elementary components, as done in Fig. 5. These plots illustrate the distribution of the electronic states near the Fermi level, E_F, as well as the valence and conduction band regions. Firstly, the projected DOS (PDOS) shows O dominancy in the valence band (from *ca.* −6 to 0 eV with respect E_F), consistent with its high electronegativity and electron affinity, reflecting its role as the primary bonding element. In more detail, the contributions near E_F arise from the hybridization of O 2p orbitals with In orbitals. Furthermore, In 5s and 5p electrons contribute significantly to the valence band, where a strong hybridization between In and O atomic orbitals agrees with the formation of In–O bonds with partial covalent character, as discussed in a previous work.[49] However, near E_F, the hybridization becomes weaker as In is partially oxidized with a concomitant depletion of its 5s/5p orbitals. In the conduction band region, a higher degree of hybridization is observed between the 5s/5p orbitals of indium and the 2p orbitals of oxygen.

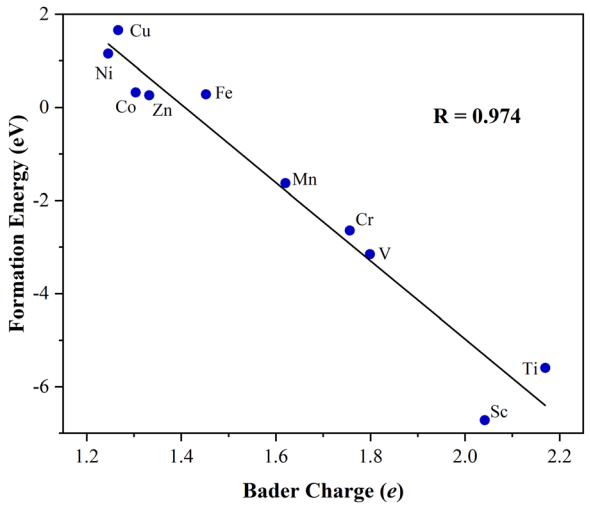

Fig. 4 Linear correlation of the 3d TM doped In_2O_3 systems formation energies *vs.* the calculated Bader charges.

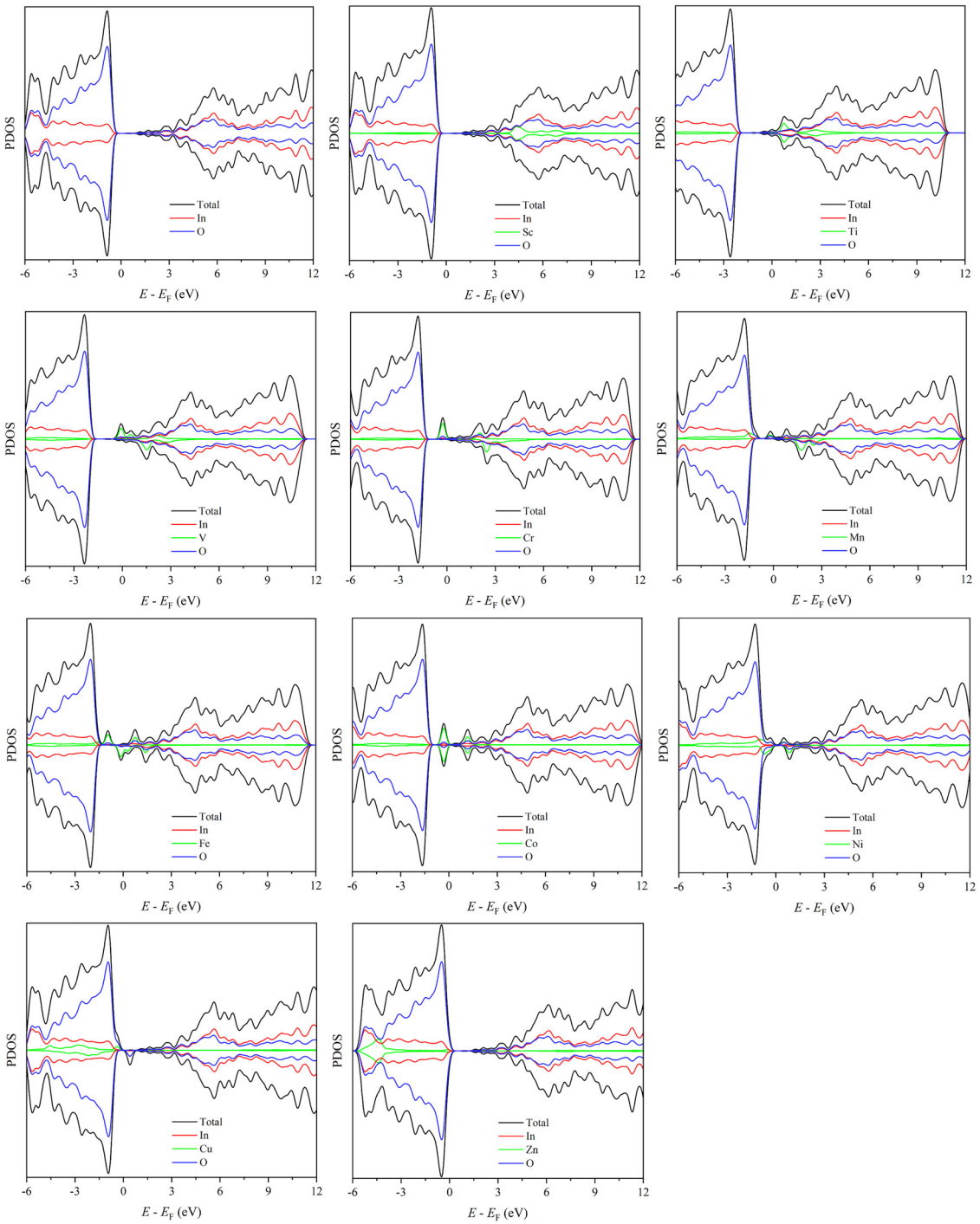

Fig. 5 Total and PDOS of the first-row transition metals-doped In_2O_3 systems. All energies are referred to Fermi energy, E_F, defined here as the maximum of the valence band.

Regarding the 3d orbital electron distributions of the TM dopants, there are significant differences, with complex peak features near E_F, reflecting the splitting of d electron energy levels and their interaction with the coordination environment. Taking the early transition metal Sc as an example, the ground-state electron configuration for the isolated atoms is $4s^23d^1$. Due to the presence of only one electron in the 3d orbital, Sc doping tends to donate 4s and 3d electron density, resulting in a lower density of state near E_F, with peaks primarily appearing in the conduction band region ($E - E_F \approx 4.5$ eV).

In contrast, Ti, V, and Cr, although being also early TMs, have more 3d electrons with a concomitant pronounced 3d states density near E_F, suggesting more active involvement of 3d electron states in charge transfer. For the late transition metals Fe and Co, their 3d orbital energy levels make a significant contribution near E_F, characterized by broad and

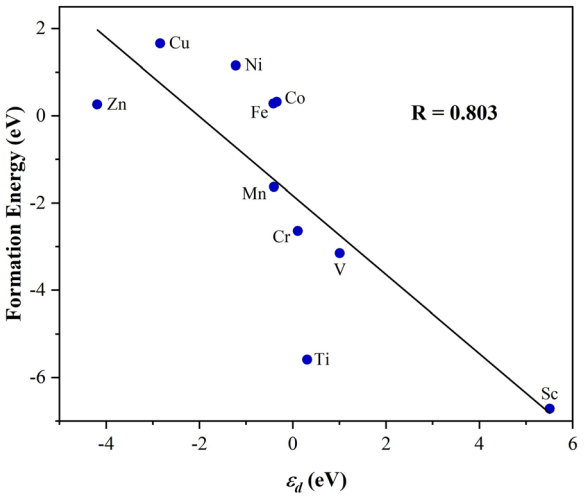

Fig. 6 Linear correlation of the 3d TM doped In_2O_3 systems formation energies *vs.* the TM ε_d values.

overlapping peaks that reflect strong hybridization between valence and conduction band edges. By contrast, Mn and Ni show relatively weaker 3d states contributions around E_F, which may be attributed to differences in their distinct electron configurations and specific orbital hybridization within the doped systems. For Mn, with its $3d^5$ high-spin configuration, the strong electron–electron repulsion leads to d-electron localization, which is consistent with the high local magnetic moment ($3.58\mu_B$) showed in Table 1. This localization may limit the orbital hybridization with neighboring atoms, resulting in a reduced d state density near E_F.[50,51] On the other hand, Ni, with its $3d^8$ configuration, experiences a quite filled 3d shell, which promotes electron localization.[52] Finally, the 3d orbitals of the late transition metals Cu and Zn exhibit typical characteristics near E_F arising from their nearly fully 3d shell, all mainly distributed in the valence band region (below E_F), with almost no contribution near E_F. This absence of 3d orbital contribution near the Fermi level is a significant feature of the electronic structure of late transition metals, especially Zn.

The d band center,[53] ε_d, calculated following the commonly accepted approach,[54] is usually employed as a descriptor in catalysis, especially for metallic surfaces[55] where this band is broad enough. Indeed, this descriptor is almost independent of the density functional used,[56] which makes it especially interesting for comparing different studies. For the present systems with a very low dopant concentration, the d band is quite narrow. Yet, its position relative to E_F may offer additional information of interest in catalysis, and the position is precisely provided by the d band center. Therefore, the d band center of the TM dopants in In_2O_3 was computed, and values listed in Table 1.

A clear correlation between ε_d values and the corresponding ΔE_f emerges as shown in Fig. 6. In general, dopants with higher d band center values tend to exhibit lower (more negative) formation energies. For instance, Sc exhibits a ε_d value of 5.51 eV and a formation energy of −6.72 eV, while Zn exhibits a ε_d of −4.19 eV and a formation energy of 0.26 eV. Nevertheless, the correlation between the d band center and formation energy is only qualitative, with an $R = 0.803$, but, in any case, indicates that the ε_d also may serve as a moderate descriptor for assessing the favorability of the doping process in In_2O_3.

The distinct PDOS features and ε_d values among different metals clearly reflect variations in hybridization characteristics and electronic structure. These results offer valuable insights for designing and selecting TM dopants with targeted stability and electronic properties.

4. Conclusions

Based on DFT, the present study systematically investigates the properties of In_2O_3 doped with the first-row TMs, with a focus put on the structural stability and main electronic structure features. The results demonstrate that the electronic configurations of the dopants strongly influence their preferred doping sites, stability, charge transfer behavior, and PDOS features of the systems. Early TMs (such as Sc, Ti, V, Cr) exhibit a pronounced thermodynamic stability, with generally negative formation energies, indicating a favorable doping. These metals would tend to substitute the relatively lower symmetry In_2 site, forming more stable coordination environments. In contrast, formation energies for metal dopants from Fe to Zn gradually increase along the 3d series, with Ni and Cu exhibiting particularly high values, indicating more unfavorable doping processes.

Bader charge analysis further revealed that a significant charge transfer from the dopant metal atoms to the In_2O_3 lattice, with a strong linear correlation between the Bader charge and formation energy, suggesting that the metal electron donating ability is a key factor governing the thermodynamic stability of the doped system. The PDOS analysis reveals that the d state density near E_F is strongly influenced by the 3d occupancy. The ε_d of the metal has been estimated and found to exhibit a moderate linear trend with the formation energy indicating that this descriptor may be useful to assess the stability of In_2O_3 systems doped with TMs, at least, in a qualitative fashion. Metals with higher ε_d, such as Sc, Ti, V and Cr, tend to form more stable systems, whereas those with lower ε_d, like Cu and Zn, are associated with higher formation energies.

This study systematically reveals the intrinsic relationships among structure, stability, and electronic properties of first-row transition metal-doped In_2O_3 systems. Specially, dopants such as Ti, V, and Cr, characterized by a high stability, strong electron transfer ability, and prominent d band states contribution near E_F, are expected to facilitate further optimization of In_2O_3-based catalysts. These findings deepen the understanding of doping regulation mechanisms and offer theoretical guidance for designing efficient CO_2 hydrogenation catalysts.

Conflicts of interest

There are no conflicts of interest to declare.

Data availability

POSCAR or CONTCAR files of the optimized structures are provided into a single zip file uploaded as additional supplementary information (SI). Supplementary information: formation energy calculated with different functionals; formation energy calculated with and without dispersion correction; high-symmetry *k*-paths in the reciprocal space of Sc-doped In_2O_3; thermodynamic properties of Sc-doped In_2O_3 as a function of temperature. See DOI: https://doi.org/10.1039/d5cp04556h.

Acknowledgements

The present work received financial support from the Spanish Ministerio de Ciencia e Innovación and Agencia Estatal de Investigación (AEI) MCIN/AEI/10.13039/501100011033 and, as appropriate, by ''European Union Next Generation EU/PRTR'', through grants TED2021-129506B-C22, PID2021-126076NB-I00, PID2024-159906NB-I00, la Unidad de Excelencia María de Maeztu CEX2021-001202-M granted to the ITQCUB and, in part, from Generalitat de Catalunya 2021SGR00079 grant. The Red Española de Supercomputación (RES projects QHS-2024-1-0001, QHS-2024-2-0014, and QHS-2024-3-0008) and Consorci de Serveis Universitaris de Catalunya (CSUC) are also acknowledged for the generous computational resources. F. V. is thankful for the ICREA Academia Award 2023 Ref. Ac2216561.

References

1 F. J. Wentz, L. Ricciardulli, K. Hilburn and C. Mears, *Science*, 2007, **317**, 233–235.
2 C. Tebaldi, R. Ranasinghe, M. Vousdoukas, D. J. Rasmussen, B. Vega-Westhoff, E. Kirezci, R. E. Kopp, R. Sriver and L. Mentaschi, *Nat. Clim. Change.*, 2021, **11**, 746–751.
3 C. Costentin, M. Robert and J.-M. Savéant, *Chem. Soc. Rev.*, 2013, **42**, 2423–2436.
4 L. Meng, L.-K. Yan, F. Viñes and F. Illas, *J. Mater. Chem. A*, 2024, **12**, 7856–7874.
5 M. D. Garba, M. Usman, S. Khan, F. Shehzad, A. Galadima, M. F. Ehsan, A. S. Ghanem and M. Humayun, *J. Environ. Chem. Eng.*, 2021, **9**, 104756.
6 A. Modak, P. Bhanja, S. Dutta, B. Chowdhury and A. Bhaumik, *Green Chem.*, 2020, **22**, 4002–4033.
7 O. Awogbemi and D. A. Desai, *Discov. Nano*, 2025, **20**, 29.
8 I. I. Maor, S. Heyte, O. Elishav, M. Mann-Lahav, J. Thuriot-Roukos, S. Paul and G. S. Grader, *Nanomaterials*, 2023, **13**, 635.
9 N. Onishi and Y. Himeda, *Acc. Chem. Res.*, 2024, **57**, 2816–2825.
10 X. Li, Q. Cheng, Y. Zhang, Y. Liu, Y. Pan, D. Zhao, S. Xiong, W. Liu, X. Jiang, J. Yan, X. Duan, Y. Tian and X. Li, *Angew. Chem., Int. Ed.*, 2025, **64**, e202424435.
11 S. Kar, R. Sen, A. Goeppert and G. K. S. Prakash, *J. Am. Chem. Soc.*, 2018, **140**, 1580–1583.
12 H. Zada, J. Yu and J. Sun, *ChemSusChem*, 2025, **18**, e202401846.
13 H. H. Wong, M. Sun, T. Wu, C. H. Chan, L. Lu, Q. Lu, B. Chen and B. Huang, *eScience*, 2024, **4**, 100140.
14 U. J. Etim, C. Zhang and Z. Zhong, *Nanomaterials*, 2021, **11**, 3265.
15 T. S. Bui, E. C. Lovell, R. Daiyan and R. Amal, *Adv. Mater.*, 2023, **35**, 2205814.
16 G. Pacchioni, *ChemPhysChem*, 2003, **4**, 1041–1047.
17 T. Pinheiro Araújo, C. Mondelli, M. Agrachev, T. Zou, P. O. Willi, K. M. Engel, R. N. Grass, W. J. Stark, O. V. Safonova, G. Jeschke, S. Mitchell and J. Pérez-Ramírez, *Nat. Commun.*, 2022, **13**, 5610.
18 L. Liu, B. Mezari, N. Kosinov and E. J. M. Hensen, *ACS Catal.*, 2023, **13**, 15730–15745.
19 F. Cannizzaro, E. J. M. Hensen and I. A. W. Filot, *ACS Catal.*, 2023, **13**, 1875–1892.
20 J. Wang, G. Zhang, J. Zhu, X. Zhang, F. Ding, A. Zhang, X. Guo and C. Song, *ACS Catal.*, 2021, **11**, 1406–1423.
21 S. Dang, B. Qin, Y. Yang, H. Wang, J. Cai, Y. Han, S. Li, P. Gao and Y. Sun, *Sci. Adv.*, 2020, **6**, eaaz2060.
22 D. Cai, Y. Cai, K. B. Tan and G. Zhan, *Materials*, 2023, **16**, 2803.
23 Z. Meng, X. Sun, Y. Tang, B. Yan, Z. Zhao and B. Li, *ChemCatChem*, 2025, **17**, e202401298.
24 Z. Ren, B. Li, Y. Wu, H. Liu, F. Guo, S. Tian and J. Yang, *Chem. Eng. J.*, 2025, **507**, 160394.
25 N. H. M. D. Dostagir, C. Thompson, H. Kobayashi, A. M. Karim, A. Fukuoka and A. Shrotri, *Catal. Sci. Technol.*, 2020, **10**, 8196–8202.
26 Z. Liu, H. Liu, M. Li, Y. Meng, X. Wang, T. Yan, Q. Fan, S. N. Lou, W. Cui and S. Zhang, *ChemCatChem*, 2024, **16**, e202301700.
27 A. Bavykina, I. Yarulina, A. J. Al Abdulghani, L. Gevers, M. N. Hedhili, X. Miao, A. R. Galilea, A. Pustovarenko, A. Dikhtiarenko, A. Cadiau, A. Aguilar-Tapia, J.-L. Hazemann, S. M. Kozlov, S. Oud-Chikh, L. Cavallo and J. Gascon, *ACS Catal.*, 2019, **9**, 6910–6918.
28 N. Wubulikasimu, R. Shen, L. Hao, H. He, K. Li, X. Li and J. Xie, *Chem. Eng. J.*, 2024, **501**, 157397.
29 M. Voccia, S. Kapse, R. Sayago-Carro, N. Gómez-Cerezo, M. Fernández-García, A. Kubacka, F. Viñes and F. Illas, *ACS Appl. Mater. Interfaces*, 2024, **16**, 30157–30165.
30 S. Kapse, F. Viñes and F. Illas, *J. Phys. Chem. C.*, 2025, **129**, 13713–13722.
31 G. Kresse and J. Furthmüller, *Phys. Rev. B: Condens. Matter Mater. Phys.*, 1996, **54**, 11169–11186.
32 G. Kresse and J. Furthmüller, *Comput. Mater. Sci.*, 1996, **6**, 15–50.
33 J. P. Perdew, K. Burke and M. Ernzerhof, *Phys. Rev. Lett.*, 1996, **77**, 3865–3868.
34 M. S. Frei, M. Capdevila-Cortada, R. García-Muelas, C. Mondelli, N. López, J. A. Stewart, D. Curulla Ferré and J. Pérez-Ramírez, *J. Catal.*, 2018, **361**, 313–321.
35 C. Sousa, S. Tosoni and F. Illas, *Chem. Rev.*, 2013, **113**, 4456–4495.
36 J. Muscat, A. Wander and N. M. Harrison, *Chem. Phys. Lett.*, 2001, **342**, 397–401.
37 I. de, P. R. Moreira, F. Illas and R. L. Martin, *Phys. Rev. B: Condens. Matter Mater. Phys.*, 2002, **65**, 155102.

38 K. C. Ko, O. Lamiel-García, J. Y. Lee and F. Illas, *Phys. Chem. Chem. Phys.*, 2016, **18**, 12357–12367.
39 S. L. Dudarev, G. A. Botton, S. Y. Savrasov, C. J. Humphreys and A. P. Sutton, *Phys. Rev. B: Condens. Matter Mater. Phys.*, 1998, **57**, 1505–1509.
40 P. E. Blöchl, *Phys. Rev. B: Condens. Matter Mater. Phys.*, 1994, **50**, 17953–17979.
41 G. Kresse and D. Joubert, *Phys. Rev. B: Condens. Matter Mater. Phys.*, 1999, **59**, 1758–1775.
42 S. Grimme, J. Antony, S. Ehrlich and H. Krieg, *J. Chem. Phys.*, 2010, **132**, 154104.
43 A. Togo and I. Tanaka, *Scr. Mater.*, 2015, **108**, 1–5.
44 J. Ederth, P. Johnsson, G. A. Niklasson, A. Hoel, A. Hultåker, P. Heszler, C. G. Granqvist, A. R. van Doorn, M. J. Jongerius and D. Burgard, *Phys. Rev. B: Condens. Matter Mater. Phys.*, 2003, **68**, 155410.
45 G. B. González, J. B. Cohen, J. H. Hwang, T. O. Mason, J. P. Hodges and J. D. Jorgensen, *J. Appl. Phys.*, 2001, **89**, 2550–2555.
46 A. Markovits, J. C. Paniagua, N. López, C. Minot and F. Illas, *Phys. Rev. B: Condens. Matter Mater. Phys.*, 2003, **67**, 115417.
47 P. Janthon, S. M. Kozlov, F. Viñes, J. Limtrakul and F. Illas, *J. Chem. Theory Comput.*, 2013, **9**, 1631–1640.
48 P. Janthon, S. Luo, S. M. Kozlov, F. Viñes, J. Limtrakul, D. G. Truhlar and F. Illas, *J. Chem. Theory Comput.*, 2014, **10**, 3832–3839.
49 S. Kapse, M. Voccia, F. Viñes and F. Illas, *J. Mol. Model.*, 2024, **30**, 161.
50 T. Paiva, G. Esirgen, R. T. Scalettar, C. Huscroft and A. K. McMahan, *Phys. Rev. B: Condens. Matter Mater. Phys.*, 2003, **68**, 195111.
51 N. U. Din, T. Jiang, S. Gholam-Mirzaei, M. Chini and V. Turkowski, *J. Phys.: Condens. Matter*, 2020, **32**, 475601.
52 N. A. Dodd, Y. Cao, J. Bacsa, E. C. Towles, T. G. Gray and J. P. Sadighi, *Inorg. Chem.*, 2022, **61**, 16317–16324.
53 B. Hammer and J. K. Nørskov, *Surf. Sci.*, 1995, **343**, 211–220.
54 I. Demiroglu, Z. Y. Li, L. Piccolo and R. L. Johnston, *Catal. Sci. Technol.*, 2016, **6**, 6916–6931.
55 J. K. Nørskov, T. Bligaard, J. Rossmeisl and C. H. Christensen, *Nat. Chem.*, 2009, **1**, 37–46.
56 L. Vega, B. Martínez, F. Viñes and F. Illas, *Phys. Chem. Chem. Phys.*, 2018, **20**, 20548–20554.